The Effects of Topography on Sea and Land Breezes in a Two-Dimensional Numerical Model

Ytzhaq Mahrer

Department of Environmental Sciences, University of Virginia, Charlottesville 22903

Roger A. Pielke

Center for Advanced Studies, Department of Environmental Sciences, University of Virginia, Charlottesville 22903

ABSTRACT

A mathematical two-dimensional hydrostatic model has been employed for the study of mesoscale circulations which develop over a mountain barrier, a flat coastline and a mountainous coastline when the prevailing flow is zero. One of the main features of the model is the inclusion of the parameterization of the surface heat budget, and shortwave and longwave radiative fluxes. Results show that the combined sea breeze and mountain circulations produce a more intense circulation during both day and night than when they act separately. The mountainous coastline case generates an inland penetrating sea breeze which develops a leeside cell of upward vertical velocity. The predictions are in qualitative agreement with the observed phenomenon.

1. Introduction

Linear and nonlinear sea and land breeze models have been extensively studied in the past by Defant (1951), Pearce (1955), Fisher (1961), Estoque (1961, 1962), McPherson (1970), Neumann and Mahrer (1971, 1974, 1975), Pielke (1974), Physick (1976) and others. In each of these models the land surface was prescribed to be flat. In reality most coastal areas are surrounded by hills and mountain barriers whose effect on the development and movement of the sea breeze convergence zones must be considered.

The purpose of this paper is to study the combined terrain and sea breeze effect in a two-dimensional, hydrostatic, primitive equation model. It is assumed that initially the atmosphere is at rest with the meteorological variables being uniform along *horizontal* planes (not along the terrain-following coordinate). Land surface temperature is calculated from the heat balance equation using a Newton-Raphson iteration technique, while sea temperature is kept constant during the integration. Radiative cooling/heating is also incorporated in the model as it plays an important role in the development of the flows, acting in a similar way to vertical turbulent mixing in diffusing atmospheric heat. When winds are calm the frictional loss of energy is small, yet the radiation effects can still be significant. Neumann and Mahrer (1971, 1974, 1975) were able to initiate a land breeze by limiting the minimum value of the vertical eddy diffusion. In this

study land and sea breezes as well as mountain and valley winds can be *initiated*, independent of the value of the eddy diffusion.

Three cases are discussed:

- Sea and land breeze over a flat terrain
- Mountain and valley winds
- The combined effects of sea, land and mountain winds.

2. Basic equations

The hydrostatic two-dimensional equations of motion, heat, moisture and continuity in the terrain-following coordinate system (x,z^*,t) are as follows (symbols defined in the Appendix):

$$\frac{du}{dt} = fv - fV_0 - \theta\frac{\partial \pi}{\partial x} + g\frac{z^* - \bar{s}}{\bar{s}}\frac{\partial z_G}{\partial x} - g\frac{z^*}{\bar{s}}\frac{\partial s}{\partial x}$$

$$+ \left(\frac{\bar{s}}{s - z_G}\right)^2 \frac{\partial}{\partial z^*}\left(K_z^m \frac{\partial u}{\partial z^*}\right) + \frac{\partial}{\partial x}\left(K_H \frac{\partial u}{\partial x}\right), \quad (1)$$

$$\frac{dv}{dt} = -fu + fU_0 + \left(\frac{\bar{s}}{s - z_G}\right)^2 \frac{\partial}{\partial z^*}\left(K_z^m \frac{\partial v}{\partial z^*}\right)$$

$$+ \frac{\partial}{\partial x}\left(K_H \frac{\partial v}{\partial x}\right), \quad (2)$$

$$\frac{d\theta}{dt}=\left(\frac{\bar{s}}{s-z_G}\right)^2\frac{\partial}{\partial z^*}\left(K_z^\theta\frac{\partial\theta}{\partial z^*}\right)+\frac{\partial}{\partial x}\left(K_H\frac{\partial\theta}{\partial x}\right),\tag{3}$$

$$\frac{dq}{dt}=\left(\frac{\bar{s}}{s-z_G}\right)^2\frac{\partial}{\partial z^*}\left(K_z^q\frac{\partial q}{\partial z^*}\right)+\frac{\partial}{\partial x}\left(K_H\frac{\partial q}{\partial x}\right),\tag{4}$$

$$\frac{\partial u}{\partial x}+\frac{\partial w^*}{\partial z^*}-\frac{1}{s-z_G}\frac{\partial z_G}{\partial x}u+\frac{1}{s-z_G}\left(\frac{\partial s}{\partial t}+u\frac{\partial s}{\partial x}\right)=0,\tag{5}$$

$$\frac{\partial\pi}{\partial z^*}=\frac{s-z_G}{\bar{s}}\frac{g}{\theta},\tag{6}$$

where

$$\left.\begin{array}{l}z^*=\bar{s}\dfrac{z-z_G}{s-z_G}\\[2ex]\pi=c_p\left(\dfrac{p}{p_{00}}\right)^{R/c_p}\\[2ex]K_H=0.36(\Delta x)^2\left[\left(\dfrac{\partial u}{\partial x}\right)^2+0.5\left(\dfrac{\partial v}{\partial x}\right)^2\right]^{\frac{1}{2}}\end{array}\right\},\tag{7}$$

$$w^*=\frac{\bar{s}}{s-z_G}w-\frac{z^*}{s-z_G}\left(\frac{\partial s}{\partial t}+u\frac{\partial s}{\partial x}\right)+\frac{z^*-\bar{s}}{s-z_G}u\frac{\partial z_G}{\partial x},\tag{8}$$

and

$$\frac{d}{dt}=\frac{\partial}{\partial t}+u\frac{\partial}{\partial x}+w^*\frac{\partial}{\partial z^*}.$$

For the soil layer we have

$$\frac{\partial T_s}{\partial t}=\frac{\partial}{\partial z}\left(K_s\frac{\partial T_s}{\partial z}\right),\tag{9}$$

where K_s is the soil heat diffusivity.

By integrating the continuity equation (5) from the surface to the top and assuming that $w^*=0$ at both boundaries, we obtain an equation for the material surface s, namely

$$\frac{\partial s}{\partial t}=-\frac{1}{\bar{s}}\int_0^{\bar{s}}\left\{\frac{\partial}{\partial x}[u(s-z_G)]\right\}dz^*.\tag{10}$$

3. Boundary layer

The boundary layer formulation is identical to the one described in detail in Pielke and Mahrer (1975). Over the land surface a roughness length $z_0=4$ cm is used, while over water (following Clarke, 1970) z_0 is defined as

$$z_0=0.032u_*^2/g,$$

with the condition that

$$z_0\geqslant 0.0015\text{ cm}.$$

Section 4, which deals with the surface heat budget equation and the longwave and shortwave radiative fluxes, has been presented by Mahrer and Pielke (1977), but are repeated here for reader convenience.

4. Surface energy balance

. The land surface temperature is computed by a Newton-Raphson iterative solution to the heat balance equation

$$R_S+R_L+\rho L u_*q_*+\rho c_p u_*\theta_*-\rho_s c_s K_s\frac{\partial T}{\partial z}\bigg|_G-\sigma T_G^4=0,\tag{11}$$

where R_S is the incoming solar radiation and R_L the incoming longwave radiation. The third, fourth and fifth terms are the latent, sensible and soil heat fluxes, respectively. By our definition negative θ_* and q_* specify upward flux of heat and moisture. The sixth term is the outgoing longwave radiation from the surface.[1] We will describe here, as briefly as possible, the various steps of the solution to Eq. (11). Let $F(T_G)$ be equal to the sum of the terms on the left side of (11) [usually in practice $F(T_G)\neq 0$]. If $|F(T_G)|$ is not less than ϵ (we have chosen $\epsilon=10^{-5}$), we apply the Newton-Raphson iteration process in the form

$$T_G^{m+1}=T_G^m-F(T_G)/F'(T_G).$$

Here $F'(T_G)$ is the derivative of $F(T_G)$ with respect to T_G with the assumption that ρ, u_*, q_*, ψ_1 and ψ_2 are constants. We then write θ_* as

$$\theta_*=\frac{k_0[\theta(1)-T_G(p_{00}/p_G)^{R/c_p}]}{0.74[\ln(z/z_0)-\psi_2]+0.0962(u_*z_0/\nu)^{0.45}},$$

where $\theta(1)$ is the potential temperature at the first grid point above the surface. The right term in the denominator is added to Businger's (1973) surface layer equation since his formulas require temperature and specific humidity at z_0 rather than at the surface. The expression for $\theta(z_0)$ and $q(z_0)$ as a function of u_* and θ_*, based on Zilitinkevich (1970), are

$$\theta(z_0)=\theta_G+0.0962(\theta_*/k_0)(u_*z_0/\nu)^{0.45},$$

$$q(z_0)=q_G+0.0962(q_*/k_0)(u_*z_0/\nu)^{0.45},$$

so that for $F'(T_G)$ we have

$$F'(T_G)=\frac{\rho c_p u_* k_0(p_{00}/p_G)^{R/c_p}}{\{0.74[\ln(z/z_0)-\psi_2]+0.0962(u_*z_0/\nu)^{0.45}\}}$$

$$\frac{\rho_s c_s K_s}{\Delta z_G}-4\sigma T_G^3.$$

---

[1] In these experiments the emissivity of the ground and atmosphere is assumed to be unity.

After the desired accuracy of $F(T_G)$ has been reached we stop the iteration and check the absolute change in θ_*. When the absolute change in θ_* is greater than 0.01 we recalculate θ_*, u_*, q_*, ψ_1 and ψ_2 from the surface layer equations (Pielke and Mahrer, 1975) with the new values of T_G and q_G and repeat the above procedure.

The shortwave and longwave radiation parameterizations in the model were adapted from the work of Jacobs et al. (1974) and are described below.

a. Shortwave radiation

The diurnal variation of the solar flux on a horizontal surface at the top of the atmosphere is computed from

$$S = S_0 \cos Z$$

with $\cos Z = \sin\phi \sin\delta + \cos\phi \cos\delta \cos\psi$, where ϕ is the latitude, δ the solar declination and ψ the solar hour angle. At the surface the solar radiation is obtained by using two empirical functions. The first empirical transmission function includes molecular scattering and absorption by permanent gases such as oxygen, ozone and carbon dioxide. This function, originally presented by Kondrat'yev (1969) and modified by Atwater and Brown (1974) to account for the forward Rayleigh scattering, is given by

$$G = 0.485 + 0.515\left[1.041 - 0.16\left(\frac{0.000949p + 0.051}{\cos Z} \right)^{\frac{1}{2}} \right],$$

where p is pressure (mb).

The second empirical function is from McDonald (1960) and accounts for the absorptivity of water vapor

$$a_w = 0.077\left[\frac{r(z)}{\cos Z} \right]^{0.3},$$

where r is the optical path length of water vapor above the layer z. It is given as

$$r(z) = \int_z^{\text{top}} \rho_z q_z dz.$$

The net shortwave radiative flux at the surface is

$$R_S = \begin{cases} S_0 \cos Z(1-A)(G-a_w), & \cos Z > 0 \\ 0 & , \cos Z \leqslant 0 \end{cases}$$

where A is the albedo.

The solar radiative heating rates in the atmosphere are computed for the absorption of shortwave energy by the water vapor only and are given by

$$\left(\frac{\partial T}{\partial t} \right)_S = \frac{S_0 \cos Z}{\rho c_p} \frac{\partial a_w}{\partial Z}$$

or by substitution,

$$\left(\frac{\partial T}{\partial t} \right)_S = 0.0231 \frac{S_0 \cos Z}{\rho c_p}\left[\frac{r(z)}{\cos Z} \right]^{-0.7} \frac{dr}{dz}.$$

b. Longwave radiation

Longwave radiation and atmospheric heating due to its flux divergence are calculated for each timestep. Carbon dioxide and water vapor are considered as emitters of longwave radiation. The path length for water vapor (Δr_j) is computed for each layer from the surface to the top of the model by

$$\Delta r_j = -\frac{(P_{j+1} - P_j)}{g} q_j.$$

The path length for CO_2 (Δc_j) is

$$\Delta c_j = -0.4148239(p_{j+1} - p_j).$$

After these increments are obtained they are summed up from the first level to the ith level to give the total path length, given as

$$r_i = \sum_{j=1}^{i} \Delta r_j, \quad c_i = \sum_{j=1}^{i} \Delta c_j.$$

The emissivity for water vapor was derived from data of Kuhn (1963) and is given in Jacobs et al. (1974):

$$\epsilon_r(i,j) = \begin{cases} 0.11288 \log_{10}(1+12.63\bar{r}) & \text{for } \log_{10}\bar{r} < -4 \\ 0.104 \log_{10}\bar{r} + 0.440 & \text{for } \log_{10}\bar{r} < -3 \\ 0.121 \log_{10}\bar{r} + 0.491 & \text{for } \log_{10}\bar{r} < -1.5 \\ 0.146 \log_{10}\bar{r} + 0.527 & \text{for } \log_{10}\bar{r} < -1 \\ 0.161 \log_{10}\bar{r} + 0.542 & \text{for } \log_{10}\bar{r} < 0 \\ 0.136 \log_{10}\bar{r} + 0.542 & \text{for } \log_{10}\bar{r} > 0 \end{cases}$$

Here $\bar{r} = |r_i - r_j|$ is the optical path length between the ith and jth levels.

Kondrat'yev's (1969) emissivity function for carbon dioxide is used in the form

$$\epsilon_{CO_2}(i,j) = 0.185[1 - \exp(-0.3919|c_i - c_j|^{0.4})].$$

Finally the emissivity at each level is given by

$$\epsilon(i,j) = \epsilon_r(i,j) + \epsilon_{CO_2}(i,j).$$

Using the above emissivity functions we have for the downward and upward fluxes at a level N

$$R_d(N) = \sum_{j=N}^{\text{top}-1} (\sigma/2)(T_{j+1}^4 + T_j^4)[\epsilon(N, j+1) - \epsilon(N,j)]$$

$$+ \sigma T_{\text{top}}^4[1 - \epsilon(N, \text{top})]$$

and

$$R_u(N) = \sum_{j=1}^{N-1} (\sigma/2)(T_{j+1}{}^4 + T_j{}^4)[\epsilon(N,j) - \epsilon(N, j+1)] + \sigma T_G{}^4[1 - \epsilon(N,0)].$$

The radiative cooling at each level is computed from

$$\left(\frac{\partial T}{\partial t}\right)_N = \frac{1}{\rho c_p} \frac{[R_u(N+1) - R_u(N) + R_d(N) - R_d(N+1)]}{z(N+1) - z(N)}. \tag{12}$$

Since the above procedure consumes a large amount of computation time we adopted Sasamori's (1972) technique which assumes that the whole atmosphere has the temperature of the level at which flux divergence is calculated. In this way the radiative cooling is approximated by

$$\left(\frac{\partial T}{\partial t}\right)_N = \frac{1}{\rho c_p[z(N+1) - z(N)]}\{(\sigma T_N{}^4 - \sigma T_G{}^4)$$

$$\times [\epsilon(N+1, 0) - \epsilon(N,0)] + (\sigma T_{top}{}^4 - \sigma T_N{}^4)$$

$$\times [\epsilon(N+1, top) - \epsilon(N,top)]\}. \tag{13}$$

We have compared results using both (12) and (13) to compute temperature changes due to the longwave radiative flux divergence and found only negligible differences in the results.

c. *The terrain effects on radiation*

Kondrat'yev (1969) gives the following expression for the solar radiation on a slant surface:

$$S_{sl} = S_0 \cos i,$$

where i is the angle of incidence of solar rays on the inclined surface, and

$$\cos i = \cos\alpha \cos Z + \sin\alpha \sin Z \cos(S - \eta).$$

Here α is the slope angle, Z the zenith angle, and β and η are solar and slope azimuths:

$$\alpha = \tan^{-1}\left[\left(\frac{\partial z_G}{\partial x}\right)^2 + \left(\frac{\partial z_G}{\partial y}\right)^2\right],$$

$$\beta = \sin^{-1}\left(\frac{\cos\delta \sin\psi}{\sin Z}\right),$$

$$\eta = \tan^{-1}\left(\frac{\partial z_G}{\partial y} \Big/ \frac{\partial z_G}{\partial x}\right) - \frac{\pi}{2}.$$

For a slant surface the solar and infrared radiation will be modified to

$$R_S|_{sl} = R_S \frac{\cos i}{\cos Z},$$

$$R_L|_{sl} = R_L \cos\alpha.$$

5. Surface vertical advection

Whenever the vertical velocity at the first layer is positive we evaluate the vertical derivatives of temperature, humidity and velocity from surface layer similarity theory. Although this theory assumes no vertical motion, we feel that the use of the theoretical profiles of the dependent variables in the surface layer is more realistic than assuming a linear gradient. The latter is required if a straightforward finite-difference approximation is used. The advection terms for this case are thus defined as

$$w_1^* \frac{\partial u}{\partial z^*} = w_1^* \frac{u_* | _x \phi_m}{k_0 z^*}, \quad w_1^* \frac{\partial v}{\partial z^*} = w_1^* \frac{u_* | _y \phi_m}{k_0 z^*}$$

$$w_1^* \frac{\partial \theta}{\partial z^*} = w_1^* \frac{\theta_* \phi_H}{k_0 z^*}, \quad w_1^* \frac{\partial q}{\partial z_*} = w_1^* \frac{q_* \phi_H}{k_0 z^*}.$$

6. Initial and boundary conditions

Since we start from an atmosphere at rest we have to insure that the pressure and topographic terms in the terrain-following coordinate system are in balance. That is, the meteorological variables must be uniform along a horizontal plane. With θ defined initially as

$$\theta(x,z^*) = \theta_0 + \gamma\{z^*[\bar{s} - z_G(x)]\bar{s}^{-1} + z_G(x)\},$$

where γ is the potential temperature lapse rate in the vertical, the two pressure terms in (1) should cancel each other. However, due to numerical truncation errors (e.g. Gary, 1973), the two terms are not exactly in balance. In an experiment with no forcing, (so that only truncation can cause motion) we were able to reduce the maximum changes in the horizontal velocity field due to the finite difference approximation of these terms to 5 cm s^{-1} in one hour. This was done by writing the pressure and topographic terms as

$$\frac{\partial \pi}{\partial x} + \frac{g}{\bar{s}} \frac{z^* - \bar{s}}{\theta} \frac{\partial z_G}{\partial x} = -\frac{\pi(I+1, J) - \pi(I-1, J)}{2\Delta x}$$

$$+ \frac{g}{\bar{s}\Delta x} \frac{[z^*(J) - \bar{s}][z_G(I+1) - z_G(I-1)]}{[\theta(I+1, J) + \theta(I-1, J)]},$$

and by calculating the pressure from (6) as follows:

$$\pi(I,J) = \pi(I, J+1) + \frac{s - z_G(I)}{\bar{s}}\left\{\frac{g}{\bar{\theta}_1}[z(J+1) - z(J+\tfrac{1}{2})] + \frac{g}{\bar{\theta}_2}[z(J+\tfrac{1}{2}) - z(J)]\right\},$$

where $\bar{\theta}_1$ is defined at $z(J+\tfrac{3}{4})$ and $\bar{\theta}_2$ at $z(J+\tfrac{1}{4})$ (notice that θ points are defined between pressure points).

The reduction in error results from a weighted partitioning of the finite-difference terms.

The boundary conditions are as follows:

$$q_G = F_w q_{G,saturated} + (1 - F_w)q(1) \Big\} \quad z^* = 0$$
$$u = v = w^* = 0$$

$$u = 0, \quad v = 0, \quad w^* = 0$$
$$\pi = \bar{\pi} - g(s - \bar{s})/[\theta(s) + \tfrac{1}{2}\gamma_{top}(s - \bar{s})] \Big\} \quad z^* = \bar{s}$$
$$q(s) = \text{constant}, \quad \theta(s) = \text{constant}.$$

Here F_w is a measure of surface wetness and γ_{top} is the potential temperature lapse rate at the top of the model. At the lateral boundaries

$$\frac{\partial}{\partial x}(\theta, \pi, z_G, s, q) = 0$$

$$u = 0, \quad v = 0.$$

In order to eliminate boundary effects a smoother of the form

$$\bar{\phi}(I, J) = 0.5\phi(I, J) + 0.25[\phi(I+1, J) + \phi(I-1, J)]$$

has been applied to the last three points in each direction.

7. Numerical aspects

A full description of the numerical procedure is given in Pielke (1974) and in Mahrer and Pielke (1975, 1976). In the horizontal we used 30 grid points with a grid interval of 7.5 km except at three points near the lateral boundaries where the grid interval was increased linearly to 30 km. In the vertical the atmosphere was divided into 12 levels with heights of 0, 5, 15, 100, 400, 900, 1500, 2000, 3600, 4000, 5000 and 6000 m. The timestep was 90 s. A bell-shaped mountain given by the function

$$z_G = H_0 B^2 / (x^2 + B^2)$$

was used with $H_0 = 900$ m and $B = 15$ km. In the soil we used 10 layers with constant grid spacing of 5 cm. In these experiments it is not necessary to grow the mountain, as performed previously (Pielke and Mahrer, 1975), since we start with a uniform potential temperature field along *horizontal* planes.

Values of the remaining input parameters are given in Table 1.

TABLE 1. Input parameters.

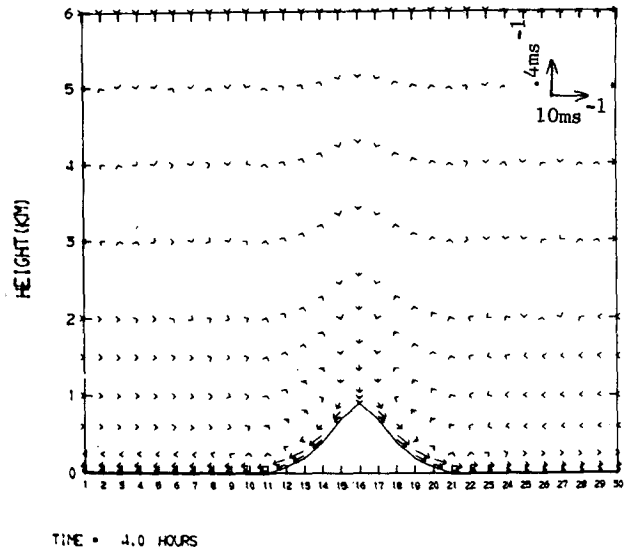|	
$F_w = 0.05$	$\phi = 33°$
$K_s = 0.03$ cm^2 s^{-1}	$\delta = 22°$
$\rho_s = 1.5$ g cm^{-3}	$\sigma = 1.38 \times 10^{-12}$ cal cm^{-2} K^{-4} s^{-1}
$C_s = 0.31$ cal g^{-1} K^{-1}	$\nu = 0.15$ cm^2 s^{-1}
$z_0 = 4$ cm (for land)	$S_0 = 0.03$ cal cm^{-2} s^{-1}
$A = 0.2$	$k_0 = 0.35$

FIG. 1. The u and w components of the wind at 0400 LST with the scale of the magnitudes given in the upper right. Note that the resolution of the speeds is different for the two components.

8. Results

In each of the following experiments the equations are integrated for 24 h starting from an atmosphere at rest at 1900 LST.

a. Mountain and valley winds

At night the mountain slope and the air in contact with it cools off more rapidly than the free atmosphere, and this differential heating generates a circulation which is called the mountain wind. The onset of the mountain winds occurs soon after sunset, and 4 h later the winds reach ·their maximum speed, remaining approximately steady throughout the night until reversing to upslope flow in the morning. The maximum strength of the mountain wind is found at a height of 15 m (Fig. 1) with a magnitude of ~ 4.0 m s^{-1}. The upper return currents are much weaker and extend up to great heights with a maximum value of 0.9 m s^{-1}. The sinking motion associated with the mountain winds is confined to the air near the mountain slopes, while compensating slow ascent is found over the flat terrain and over the slopes at higher elevations.

During the daytime excess·warming of the air near the mountain slopes relative to the free atmosphere at a corresponding level creates a pressure gradient force toward the mountain slope and causes a circulation known as the valley wind. Fig. 2 shows a vertical cross section of the u, w velocity components at 1600 LST with a maximum valley wind of ~ 5.5 m s^{-1}. The upslope wind reaches a depth of 1.0–1.5 km, in comparison to 250 m for the nighttime downslope winds. This is indicative of the destabilizing influence of the solar insolation and the resulting greater vertical mixing of heat. At night the radiative cooling acts to inhibit the
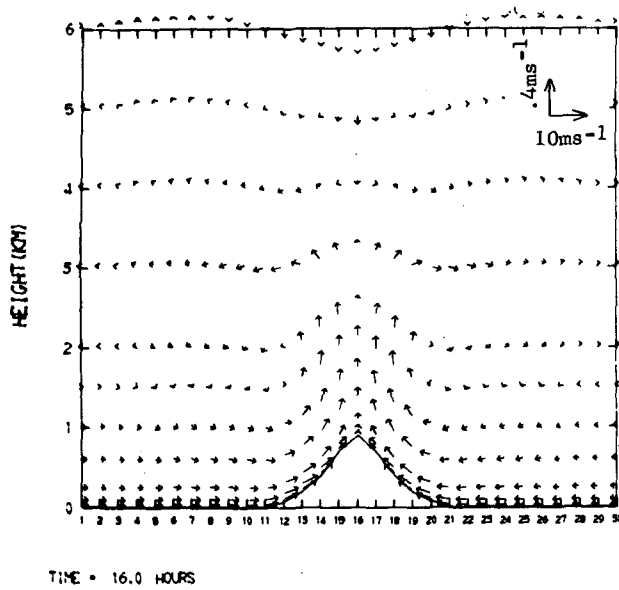
TIME • 16.0 HOURS

FIG. 2. As in Fig. 1 except for 1600 LST.

vertical diffusion and thereby limits the depth of the circulation.

The upper return circulation is found between 2 and 6 km and measures ∼1–3 m s⁻¹. The sinking air over the top of the mountain and over the open terrain occupies a much larger volume than the rising air, and the downward velocities are therefore weaker.

Fig. 3 depicts the diurnal variation of topographically induced winds at a distance of 22.5 km eastward from the top of the mountains, at a height of 5 m. During the day the east to east-southeasterly wind is prevailing due to the upslope flow, while at night the flow becomes west-northwesterly. The afternoon strengthening of the wind is evident, with the maximum occurring at about 1600 LST.

The simulated surface temperatures at a distance of 7.5 km eastward and westward from the summit, shown in Fig. 4, give a diurnal variation of 29°C. Quite striking are the early morning and late afternoon differences between the slopes, with the east slope being warmer by 1–2°C in the morning and cooler by about the same

FIG. 4. Diurnal cycle of the surface temperature at a distance of 7.5 km eastward and westward from the top of the mountain.

amount in the afternoon. With a steeper mountain the differences would have probably been larger.

Although actual values may differ, observations confirm the salient features of the pattern obtained in our calculation: for example, Defant's (1951) diagrams. MacHattie's (1968) observations in Kananaskis Valley (Alberta) and Tyson's and Preston-Whyte's (1972) report on mountain and valley winds in Natal (South Africa).
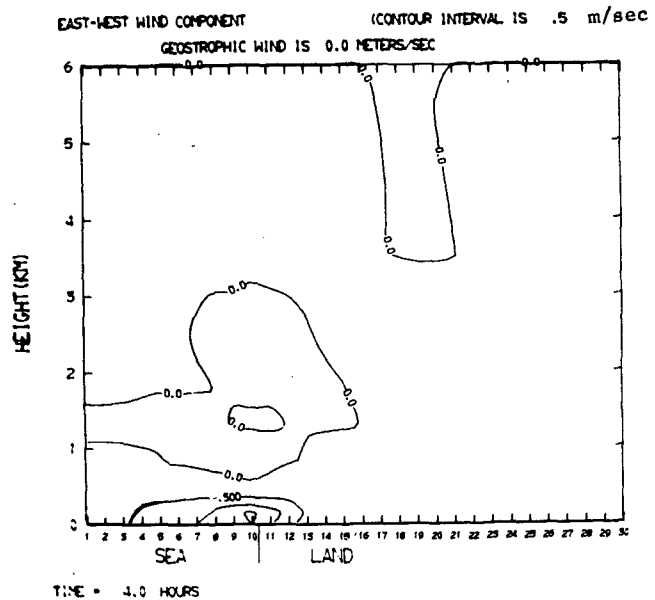

FIG. 3. Diurnal variation of the 5 m horizontal wind at a distance of 22.5 km eastward from the top of the mountain.

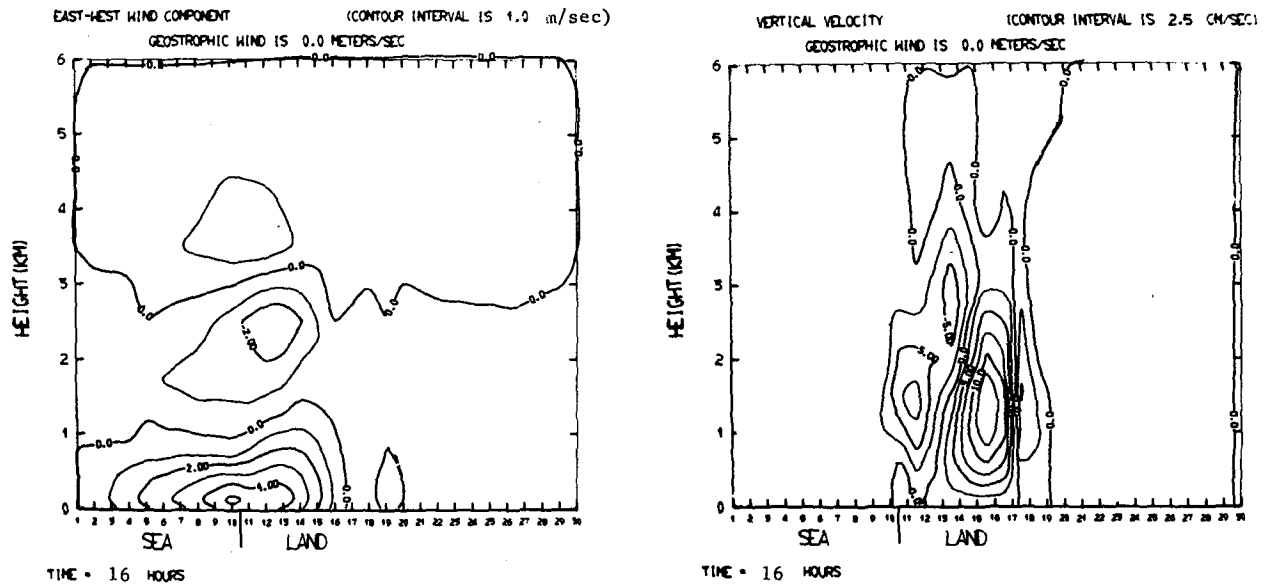FIG. 5. West-east component of the wind at 0400 LST (contour interval m s⁻¹).

FIG. 6. Left: as in Fig. 5 except for 1600 LST (contour interval is 1 m s⁻¹). Right: vertical velocity field at 1600 LST (contour interval is 2.5 cm s⁻¹). For clarity of presentation in the vertical velocity displays, several zero contours were removed in the upper part of the domain where the velocities oscillated around negligibly small values close to zero.

b. Sea and land breezes over flat terrain

The development and movement of the sea breeze convergence zones over a flat terrain have been discussed in detail in a large number of numerical models. In general the diurnal cycle of land surface temperature was prescribed. An exception is the work by Physick (1976) who added a surface heat budget equation to predict surface temperatures and found that the development of horizontal gradients of surface temperature over land resulted in a stronger thermal gradient across the sea breeze front. In this section we will give only a brief description of our results.

The land breeze at 0400 LST is shown in Fig. 5 with weak flow reaching a maximum of 1.6 m s⁻¹ at the first two levels of the model. At this time the influence of the land breeze extends a distance of 20–30 km inland. The vertical velocities associated with the land breeze are less than 1 cm s⁻¹ (not shown).

The vertical cross section of the wind at 1600 LST is shown in Fig. 6. The strongest winds are about 5 m s⁻¹, and the sea breeze front is at a distance of 40–45 km inland. The winds ahead of the front are nearly opposite in direction to that of the sea breeze, a result which is consistent with the findings of Neumann and Mahrer (1974). The maxima of the vertical velocities at this time are +15 and −8 cm s⁻¹ at a height of 1.5 km. These values are similar to those obtained in other numerical models.

Interesting results from the present study include the increase in surface temperatures as we move inland (Fig. 7), which is consistent with Physick's results, and the tendency for surface cooling after the passage of the front (i.e., 1100 LST for the 26.25 km inland curve

and after 1500 LST for the 41.25 km curve). The reduction in the rate of surface heating in the morning and the more rapid cooling in the afternoon must be due to the inland advection of cooler marine air with its stronger surface layer winds. The higher wind speeds cause increased vertical mixing of the near surface warm air as well as an enhanced cooling by evaporation of moisture from the ground. A similar result (the increase of shearing stress after the passage of the front) was obtained by Neumann and Mahrer (1974).
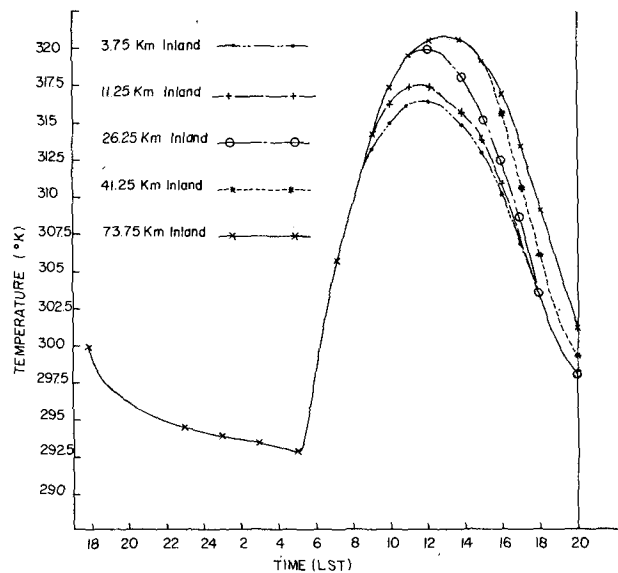

FIG. 7. Diurnal cycles of the surface temperature at variable distances from the coastline.
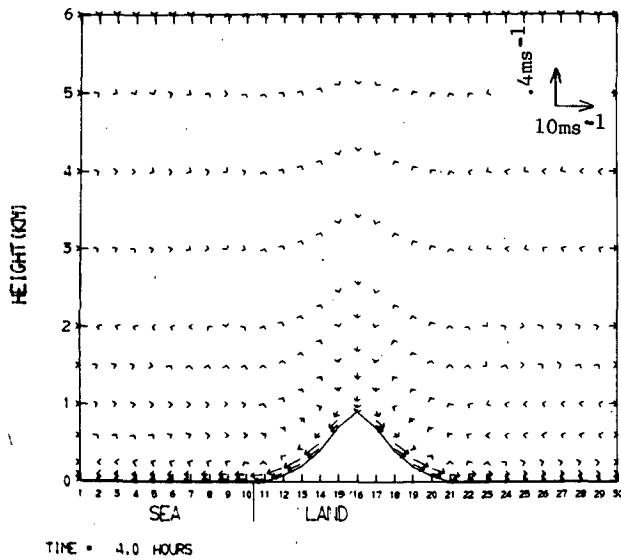
FIG. 8. The u and w components of the wind at 0400 LST.

c. Combined terrain and sea-land effects

1) NOCTURNAL FLOW

The combined effects of downslope mountain winds and the land breeze result in a stronger flow (by $\sim$1 m s^{-1}) at the western side of the mountain (Fig. 8). The maximum 15 m wind at the coast at 0400 LST is 4.0 m s^{-1} in comparison to 3 m s^{-1} in the mountain run (at the same distance from the mountain top) and to 1.6 m s^{-1} in the flat sea-land breeze experiment. This indicates that the mountain drainage caused by nocturnal surface cooling on a sloping surface accentuates the offshore pressure gradient created by the differential cooling between land and water.

2) DAYTIME FLOW

In Figs. 9–12, we show the results of the computation for 1200, 1400, 1600 and 1800 LST. The upslope valley wind during the daytime becomes integrated with the inland-advancing sea breeze; thus the flow at the west slope will be stronger than at the east slope, and will advect the eastside circulation eastward.

The sea breeze front (we will refer to it as the front) is located at the center of the mountain in the forenoon and moves eastward as the combined winds pick up. For example, at 1200 LST (Fig. 9, top), the front near the surface is found $\sim$7 km east of the mountain center, while it is 10 km east at 1400, 15 km east at 1600 and 25 km east at 1800 LST. Three major cells of vertical velocity characterize the combined flow:

    (i) A cell of upward velocity on the west side confined to the air near the slope.

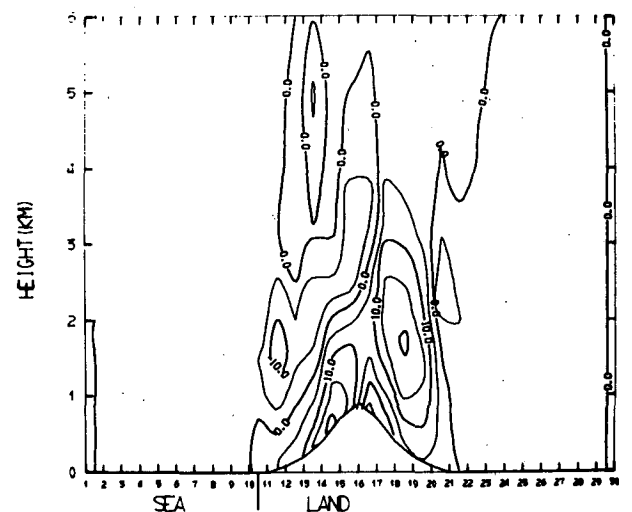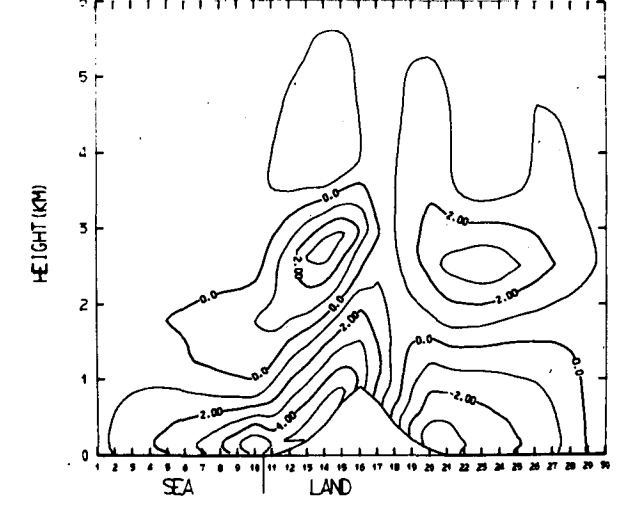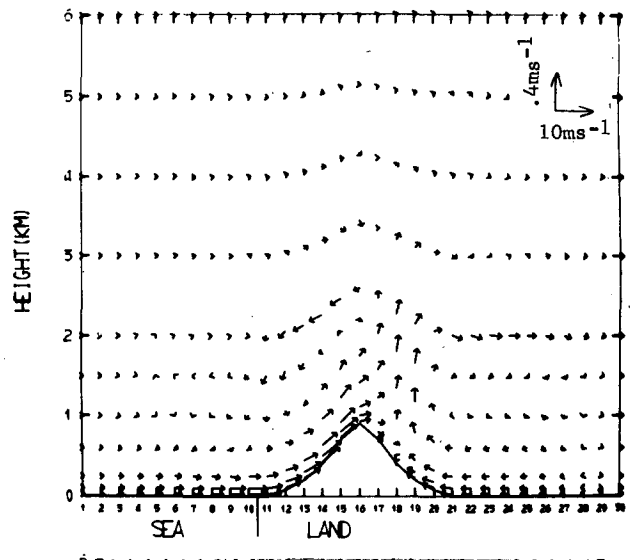   (ii) A cell of downward motion over the center of the mountain at high elevation. This cell grows

FIG. 9. The u and w components of the wind at 1200 LST (top), the west-east components (middle) (contour interval is 1 m s^{-1}) and the vertical velocity field (bottom) (contour interval is 5 cm s^{-1}).

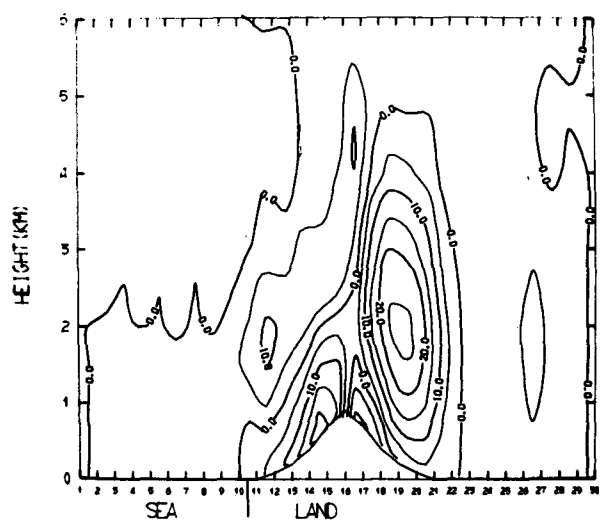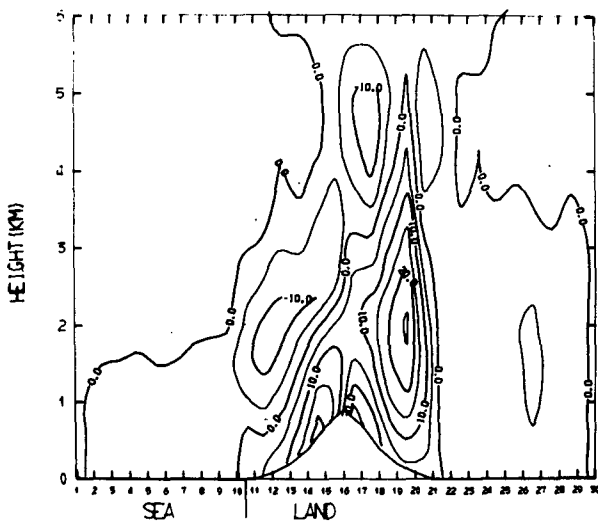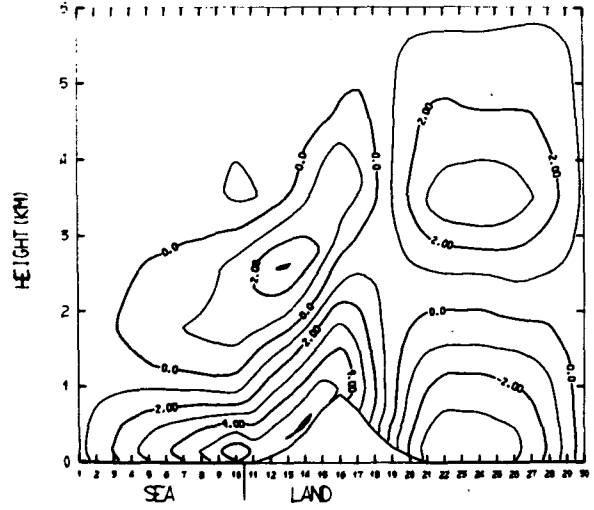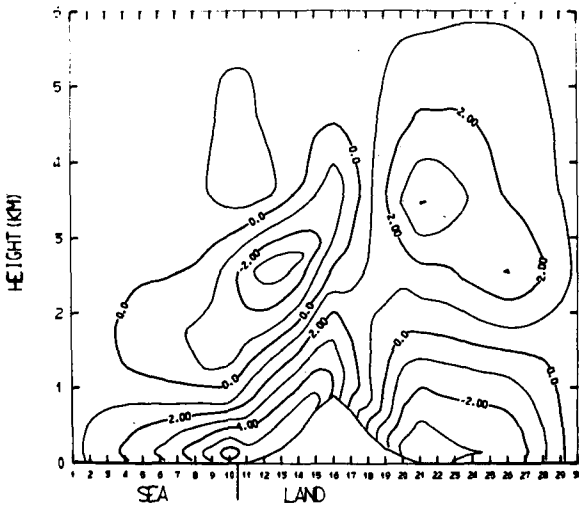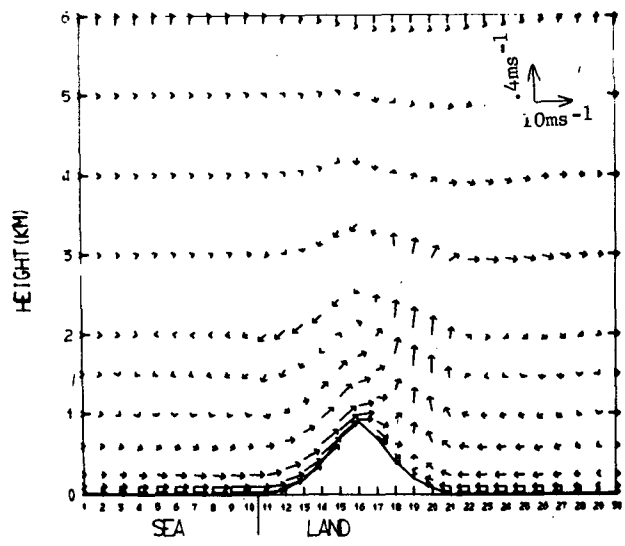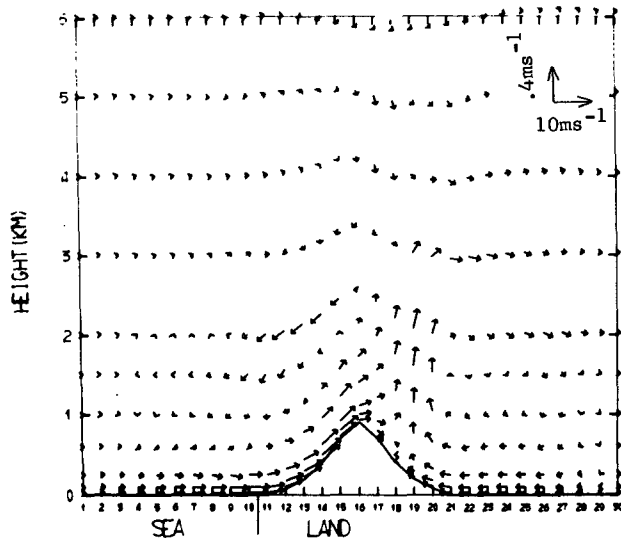FIG. 10. As in Fig. 9 except for 1400 LST.
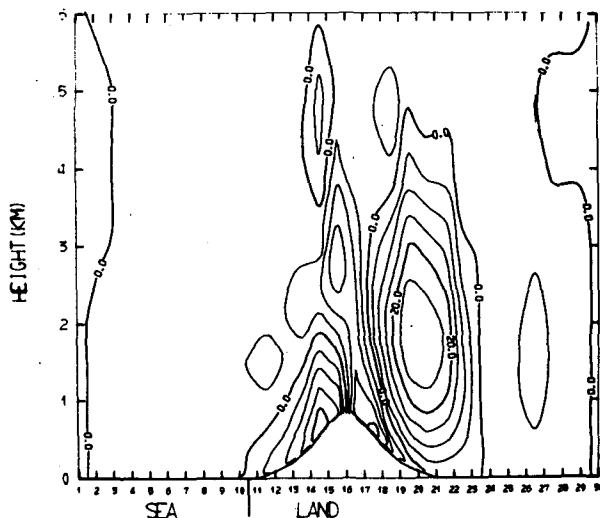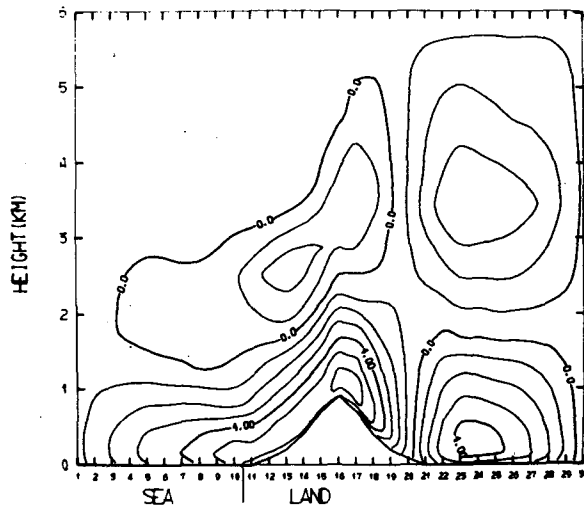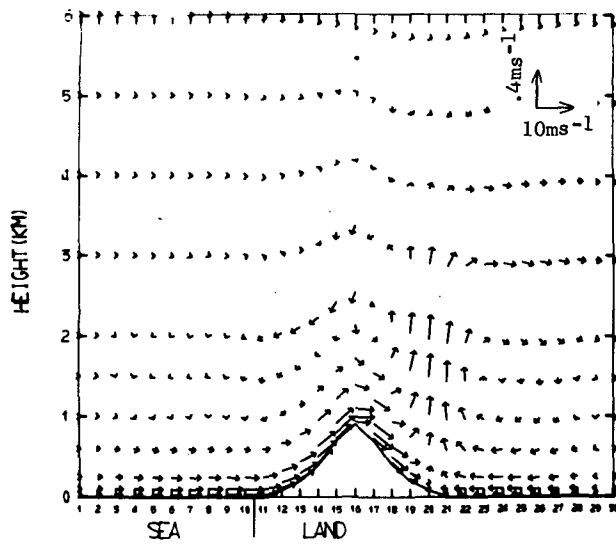
FIG. 11. As in Fig. 9 except for 1600 LST.

FIG. 12. As in Fig. 9 except for 1800 LST.

substantially with the movement of the front until it covers a part of the eastern slope.

(iii) A cell of upward motion near and over the east slope. In the early hours of the day this cell was restricted to the air near the slope, but with the penetration of the front inland the cell moved inland increasing both in size and in magnitude.

A cell of upward velocity similar to that listed in (iii) is observed downwind of the island of Barbados (De Souza, 1972). In the case presented here the advection of a heated plume downstream by the sea breeze is similar to the advection of a temperature maximum downwind by the synoptic wind such as reported by Mahrer and Pielke (1976, 1977) for Barbados and for an area of mountainous terrain in the White Sands Missile Range of New Mexico.

Other features of major interest are the diurnal changes of wind direction at the eastern slope. Fig. 13 shows the 5 m wind at a distance of 15 km east of the mountain for selected hours. By nighttime the winds are west-northwesterly, while by day they change from east-southeasterly in the forenoon hours to north-westerly during the afternoon. A similar change in wind direction is observed near Lake Kineret and the Dead Sea in Israel (J. Neumann, personal communication). Although the topographical features are not identical, the general shape of that area resembles, to some extent, the case studied here.

Three-dimensional experiments are underway to compare in more detail the predictions with the improved form of the model against observations for selected case studies.

9. Conclusion

In this paper, a two-dimensional model using parameterization of the surface heat budget and short-wave and longwave radiative fluxes was utilized to investigate the circulations which develop over a mountain barrier, a flat coastline and a mountainous
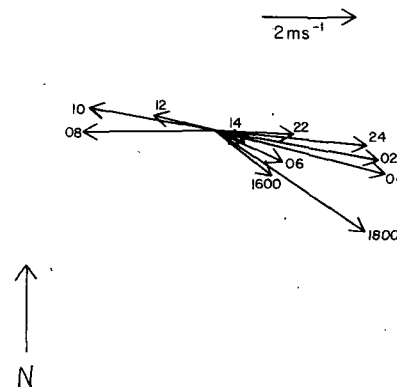

FIG. 13. Diurnal variation of the 5 m wind at a distance of 15 km eastward from the top of the mountain.

coastline, each in the absence of a large-scale prevailing flow. It was found that the sea breeze and mountain circulations acting together produce a more intense circulation during the day and night, than they do acting separately. The predicted patterns are in qualitative agreement with existing observations, and support the application of this type of model to actual geographic regions.

APPENDIX

List of Symbols

A	surface albedo
c	optical path length for CO_2
c_p	specific heat at constant pressure
c_s	specific heat of soil
f	Coriolis parameter
F_w	moisture parameter
g	acceleration of gravity
k_0	von Kármán's constant
K_H	horizontal exchange coefficient
K_s	soil heat diffusivity
K_z^m, K_z^θ, K_z^q	vertical exchange coefficient of momentum, heat and moisture
L	latent heat
p	pressure
P_{00}	reference pressure
q	specific humidity
r	optical path length of water vapor
R	gas constant for dry air
R_L	longwave radiative flux at the surface
R_S	shortwave radiative flux at the surface
$\bar{s}$	initial height of the material surface
s	material surface top of the model
S_0	solar constant
T	temperature
u, v, w	east-west, north-south and vertical component of velocity
u_*	surface friction velocity
w^*	vertical (z^*) component of velocity
x, y, z	Cartesian coordinates
z^*	vertical, terrain-following coordinate
z_G	ground elevation
z_0	roughness parameter
Z	zenith angle

π	Exner's function $[=c_p(P/P_{00})^{R/c_p}]$
θ	potential temperature
θ_*	surface friction temperature
α	slope angle
β	solar azimuth
δ	solar declination
ρ	density
σ	Stefan-Boltzman constant
ϕ	latitude
ψ	solar hour
η	slope azimuth
ν	kinematic viscosity of air
ϵ	emissivity function
ψ_1, ψ_2	variables in the surface layer parameterization

Subscripts G and s denote ground and soil values, respectively.

REFERENCES

Atwater, M. A., and P. S. Brown, Jr., 1974: Numerical calculation of the latitudinal variation of solar radiation for an atmosphere of varying opacity. *J. Appl. Meteor.*, **13**, 289–297.

Businger, J. A. 1973: Turbulent transfer in the atmospheric surface layer. *Workshop in Micrometeorology*, Amer. Meteor. Soc., Chap. 2.

Clarke, R. H., 1970: Recommended methods for the treatment of the boundary layer in numerical models. *Aust. Meteor. Mag.*, **18**, 51–73.

Defant, F., 1951: Local winds. *Compendium of Meteorology*. Amer. Meteor. Soc., 655–672.

DeSouza, R. L., 1972: A study of atmospheric flow over a tropical island. Ph.D. dissertation, Florida State University, 203 pp.

Estoque, M. A., 1961: A theoretical investigation of the sea breeze. *Quart. J. Roy. Meteor. Soc.* **87**, 136–146.

——, 1962: The sea breeze as a function of the prevailing synoptic situation. *J. Atmos. Sci.*, **19**, 244–250.

Fisher, E. L., 1961: A theoretical study of the sea breeze. *J. Meteor.*, **18**, 216–233.

Gary, J. M., 1973: Estimate of truncation error in transformed coordinate, primitive equation atmospheric models. *J. Atmos. Sci.*, **30**, 223–233.

Jacobs, C. A., J. P. Pandolfo and M. A. Atwater, 1974: A description of a general three dimensional numerical simulation model of a coupled air-water and/or air-land boundary layer. IFYGL Final Report, CEM Rep. No. 5131-509a, Center for the Environment and Man, Hartford, Conn., 85 pp.

Kondrat'yev, J., 1969: *Radiation in the Atmosphere*. Academic Press, 912 pp.

Kuhn, P. M., 1963: Radiometeorsonde observations of infrared flux emissivity of water vapor. *J. Appl. Meteor.*, **2**, 368–378.

MacHattie, L. B., 1968: Kananaskis valley winds in summer. *J. Appl. Meteor.*, **7**, 348–352.

Mahrer, Y., and R. A. Pielke, 1975: A numerical study of the air flow over mountains using the two-dimensional version of the University of Virginia mesoscale model. *J. Atmos. Sci.*, **32**, 2144–2155.

——, and ——, 1976: Numerical simulation of the airflow over Barbados. *Mon. Wea. Rev.*, **104**, 1392–1402.

——, and ——, 1977: A numerical study of the air flow over irregular terrain. *Beitr. Phys. Atmos.* (in press).

McDonald, J. E., 1960: Direct absorption of solar radiation by atmospheric water vapor. *J. Meteor.*, **17**, 319–328.

McPherson, R. D., 1970: A numerical study of the effect of a coastal irregularity on the sea breeze. *J. Appl. Meteor.*, **9**, 767–777.

Neumann, J., and Mahrer, 1971: A theoretical study of the sea and land breezes circulation. *J. Atmos. Sci.*, **28**, 534–542.

——, and ——, 1974: A theoretical study of the sea and land breezes of circular islands. *J. Atmos. Sci.*, **31**, 2027–2039.

——, and ——, 1975: A theoretical study of the lake and land breezes of circular lakes. *Mon. Wea. Rev.*, **103**, 474–485.

Pearce, R. P., 1955: The calculation of a sea-breeze circulation in terms of the differential heating across the coastline. *Quart. J. Roy. Meteor. Soc.*, **81**, 351–381.

Physick, W., 1976: A numerical model of the sea-breeze phenomenon over a lake or gulf. *J. Atmos. Sci.*, **33**, 2107–2135.

Pielke, R. A., 1974: A three-dimensional numerical model of the sea and land breezes over south Florida. *Mon. Wea. Rev.*, **102**, 115–139.

——, and Y. Mahrer, 1975: Technique to represent the heated-planetary boundary layer in mesoscale models with coarse vertical resolution. *J. Atmos. Sci.*, **32**, 2288–2308.

Sasamori, T., 1972: A linear harmonic analysis of atmospheric motion with radiative dissipation. *J. Meteor. Soc. Japan*, **50**, 505–518.

Tyson, P. D., and R. A. Preston-Whyte, 1972: Observations of regional topographically-induced wind system in Natal. *J. Appl. Meteor.*, **11**, 643–650.

Zilitinkevich, S. S., 1970: *Dynamics of the Atmospheric Boundary Layer.* Leningrad, Gidrometeor., 291 pp.